PREDICTIVE MODELING OF INORGANIC 3C-SiC FRICTION MATERIALS USING MOLECULAR DYNAMICS SIMULATION

Yizhan Zhang, Cortney LeNeave, & Yun-Bo Yi*

Department of Mechanical & Materials Engineering, University of Denver, Denver, Colorado 80208, United States

*Address all correspondence to: Yun-Bo Yi, Department of Mechanical & Materials Engineering, University of Denver, Denver, Colorado 80208, United States, E-mail: Yun-Bo.Yi@du.edu

Original Manuscript Submitted: 3/11/2022; Final Draft Received: 7/12/2022

Metallic friction materials currently used in industry may adversely impact the environment. Substitutions for metals in friction materials, on the other hand, can introduce operational safety issues and other unforeseeable problems such as thermal-mechanical instabilities. In this work, a molecular dynamics model has been developed for investigating the effects of material composition, density, and surface asperities on the tribological properties of inorganic 3C-SiC under various contact conditions at the atomic level. Predictions on the following results have been made: (1) elastic modulus, (2) tensile strength, (3) thermal conductivity, and (4) friction coefficient. The research findings can help improve the design of metal-free friction materials against thermal-mechanical failures. Parametric studies were performed by varying a number of conditions including (1) ambient temperature, (2) sliding speed, (3) crystal orientation, (4) asperity size, (5) degree of asperity intersection, (6) types of loading, and (7) surface contact. Plastic deformation and material transfer were successfully modeled between two sliding pairs. Some of the computational results were validated against existing experimental data found in the literature. The evaluation of wear rate was also incorporated. The model can easily be extended to deal with other nonmetallic friction composites.

KEY WORDS: molecular dynamics, tribological properties, silicon carbide, metal-free friction material

1. INTRODUCTION

Friction materials are widely used in aircraft, railway, automotive, mining, agricultural, and military applications. Depending on the application, friction material formulations typically consist of phenolic resin, ceramics, carbon fibers, graphitics, metals, and metal alloys to achieve better performance in areas such as wear resistance, thermal stability, and mechanical strength (Lu, 2006; Sriwiboon et al., 2018). Most automotive brake pads contain copper particles to reduce localized overheating due to copper's excellent thermal conductivity (Solomon et al., 2007; Sanguineti et al., 2018). The existing laws and regulations in some regions (e.g., in California) require copper and other heavy metals in automotive brake pads to be phased out, reducing contamination of water systems by metal particulates from wornout brakes. Graphite, carbon fibers, and ceramics are among potential replacements for metals in friction materials. However, implementation of these nonmetallic materials may introduce operational safety issues. For instance, a disturbance in the brake contact pressure can change the rate of frictional heating and the level of thermal stresses that lead to thermal-mechanical instabilities (TMI) (Yi, 2014; Zhao et al., 2013). Hence it is critical to understand how the material properties affect the thermal-mechanical responses to prevent these new materials from failure. With this consideration, a computational experiment using molecular dynamics (MD) is a good solution. Using MD simulation, it is faster to achieve a realistic experiment environment and explore a wide array of material properties on a small scale compared to real-world experiments. This could effectively provide new insights on the design of novel friction materials or explain the mechanism of TMI in a more fundamental way.

In the literature the material properties of silicon carbide (SiC) were extensively studied due to its high toughness and its ability to withstand high temperatures. For example, Zhou et al. (2003) investigated experimentally the

tribological properties of SiC and the effect of the addition of graphite on the microscale. Wang et al. (2008) reported the nanomechanical behavior of [111]-oriented SiC nanowires using MD simulations. Mao et al. (2018) focused on the point defect effects on the thermal conductivity of β -SiC in MD simulation and found a decrease trend of thermal conductivity with the increase of the concentration of certain point defects. Li et al. (2019) tested the point defects and grain boundary effects on tensile strength and Young's modulus of 3C-SiC. Zhang et al. (2020) summarized that the tribological performance of SiC ceramics is affected by many factors such as microstructural characteristics, self-lubrication, and surface modification. However, a systematic way to investigate the tribological, mechanical, and thermal properties of friction materials via a multiscale approach is lacking in the literature.

In the current work, we studied the tribological properties of 3C-SiC as a nonmetallic friction material using MD simulation. We believe that the research lays the groundwork for studying the fundamental mechanisms of TMI involved in high-speed sliding systems. In this investigation, Large-scale Atomic/Molecular Massively Parallel Simulator, or LAMMPS (Plimpton, 1995), a classical MD code, has been used to characterize the tribological properties of SiC with the assistance of the visualization software Ovito (Stukowski, 2010).

2. METHODOLOGY

2.1 Simulation of Dry Friction

Coulomb's law (Gao et al., 2004) describes dry friction through the following equation:

$$F = \mu N \tag{1}$$

where F is the frictional force, μ is the coefficient of friction, and N is the normal force. There are two underlying assumptions involved in the law: (1) during frictional sliding the resistive force per unit area of contact is constant. This assumption can be easily justified as it implies that any part of the contact area is representative of the whole. (2) The contact area is proportional to the normal load. This one is not always justified, but it still applies to most engineering surfaces as a result of the statistical distribution of asperity heights (Rahnejat, 2010). However, at the microscopic level, the situation may be different since the scale has been changed to deal with the atomic structure, which examines atoms or molecules; the influence of interatomic bonds and potentials cannot be ignored. The interaction between atoms produces attraction or repulsion and acts as an additional force during friction. This additional force acts like adhesion where two friction materials attract each other. This kind of contribution is proportional to the number of interatomic bonds that are broken and reformed when the surfaces of two objects slide past each other (Vadgama et al., 2015). The number of interatomic bonds is related to the contact area between the two sliding surfaces. With this extra influence, the normal force can even be negative, which means the two friction objects have a very limited contact area or a small gap between them. This is a unique phenomenon, which occurs on the atomic scale; it suggests that different results could be found when compared to a macroscale analysis.

The MD model for friction simulation focuses on the process on the atomic scale. Basically, there are two kinds of cases that describe the friction process at such a small size (Zhong et al., 2003). One case uses two asperities as research objects. The main reason is that at the macroscopic level, the contact surfaces between friction materials can be treated as ideal flat planes. However, the geometry of the surface is not smooth at an atomistic level. There could always exist some peaks and valleys but only noticeable at the micro- or nanoscale such that they are ignored in traditional macroscopic experiments. The other case uses an asperity sliding on a relatively smooth slab. A smooth surface is less common at the nano level, but it is still a possible situation. An example of the asperity friction at nanoscale in a real experiment is from Sato et al. (2012). They used a transmission electron microscope to observe the nanofriction of a single Ag asperity and recorded the shear force, shear displacement, and real contact area. Lessel et al. (2013) found that the van der Walls interactions on single asperity friction at the atomic level have noteworthy influence under different conditions. Si et al. (2015) implemented MD simulation to investigate how the number of asperities and their heights affect the frictional force and adhesive force locally and concluded that both forces increase with more asperities and decrease with larger height, but it becomes less obvious when the asperity height exceeds a critical value.

In the current work, both cases were considered. For asperity-asperity shear, the 3D model was created using upper and lower asperities, as shown in Fig. 1 through Ovito. Two hemispherical asperities were built in a cuboid

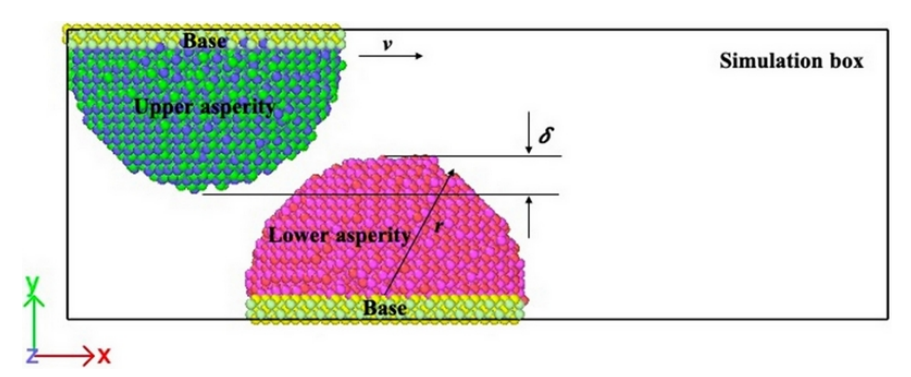


FIG. 1: Schematic of asperity-asperity SiC friction model

simulation box. Si atoms are shown in blue and red, while C atoms are shown in green and pink (the actual atomic radius of the two types of elements is not shown). One asperity is at the upper position of the box while the other is at the lower position of the box. Both asperities were connected to bases, which were also made from SiC, and were used for moving or fixing the asperities. First, the lower asperity and lower base were fixed to the initial position as exhibited in Fig. 1. Next, a constant velocity was added to the upper base to drive the corresponding upper asperity in the positive x-direction. This gives the upper asperity a relative velocity to the lower asperity. Periodic boundary conditions (PBCs) were applied in the x- and z-directions, while a nonperiodic and shrink-wrapped boundary condition was applied in the y-direction such that the faces can encompass the atoms in that direction no matter how far they move. During the simulation, a microcanonical (NVE) ensemble was applied to the asperities. In asperity-slab shear, the lower asperity was replaced with a SiC slab and the rest of the settings were kept the same. New loading was imparted on the upper base to make it move downward with the upper asperity and contact the slab, then a constant velocity was added to the upper base to make the asperity move along a positive x-direction. The designed MD model is exhibited in Fig. 2. In the asperity-slab shear simulation, the length of the slab along the x-axis was always 80 Å. In this work, only 3C-SiC (or β -SiC, zinc-blend cubic structure with lattice constant of 4.3596 Å) was considered. The timestep was set to 0.001 ps. For each timestep, the forces acting on the atoms were calculated from the derivative of the potential; the position and the velocity and were obtained using the velocity-Verlet method (Sharma, 2019).

Vashishta potential, which is used to compute the combined two-body and three-body family of potentials in inorganic compounds, was implemented for the SiC system in all the simulations in this investigation. This kind of potential is derived from the research made by Priya Vashishta et al. (2007). The basic formula for the total potential energy of the system is given by

$$E = \sum_{i < j} E_{ij}^{(2)}(r_{ij}) + \sum_{i,j < k} E_{ijk}^{(3)}(r_{ij}, r_{jk})$$
(2)

where the first and second terms represent the two-body part and three-body part of the effective potential, respectively. Specifically, $E_{ij}^{(2)}$ is the effective potential energy of two-body interactions, and $E_{ijk}^{(3)}$ is the effective potential energy of three-body interactions. r_{ij} and r_{jk} represent the distance between atom i and j and the distance between

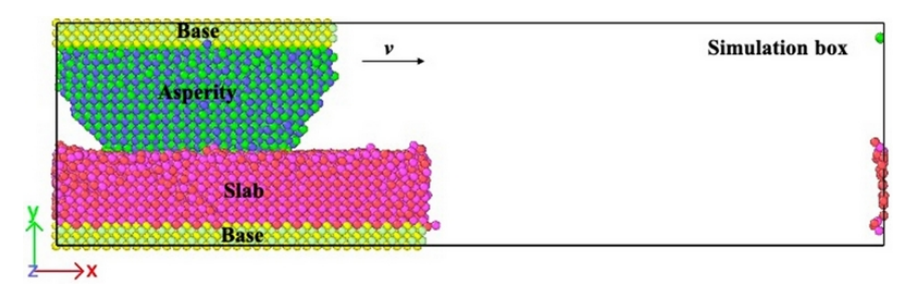


FIG. 2: Schematic of asperity-slab SiC friction model

atom *j* and *k*, respectively. Since the complex chemical bonds in SiC involve both ionic and covalent characters, the potential formula must contain a minimal steric repulsion with Coulomb interaction from two-body interactions and the covalent bond bending and stretching from three-body interactions so the overall potential profile could be better described. The initial conditions of the friction simulation were modified to investigate the effect of the temperature, sliding speed, crystal orientation, particle size, and degree of intersection on friction. The wear rate of each friction material and the total wear rate of the system for each simulation were calculated as well. It should be noted that the simulation system is in a vacuum, which means no tribochemical reaction is considered in this work.

2.2 Simulation of Mechanical Properties

In the laboratory, a tensile test may be the most common method to analyze the modulus of a sample material. The atomic-level simulation in this investigation is similar to a laboratory tensile test. In the simulation for elastic modulus evaluation, the bulk shape 3C-SiC was created because a regular shape more easily examines the relationship between stress and strain. Figure 3 is a schematic of a SiC MD model for tensile simulation. In this model, the atoms from the bottom layers, in the y-direction, of the bulk material were fixed, and a constant velocity was exerted on the top several layers, so the model was stretched with a constant strain rate until fracture or failure occurred. These two top and bottom portions were assigned to the boundary part, and the rest of the portion was assigned to the middle part. The simulation was run in a simulation box with a boundary condition of ssp (s, nonperiodic and shrink-wrapped; p, periodic) in the x-, y-, and z-directions, respectively. The tensile force direction was parallel to the y-axis. First, the entire system was relaxed at 300 K under a canonical (NVT) ensemble using several steps. Then, the NVT ensemble worked on the middle part, while the boundary part was under the NVE ensemble. After that, the stress–strain curve was drawn to calculate the final elastic modulus. To calculate the elastic modulus, the same formula involved in macroscopic experiments was used, which is shown below:

$$\sigma = E\varepsilon \tag{3}$$

In this equation, E represents elastic modulus, σ is the tensile stress, and ε is the strain. The strain can also be used to describe the area of elastic deformation under the stress–strain curve. It should also be noticed that on an atomic scale, there may be some factors that affect the precision of the computation such as the shape and the size of the model or the speed of tension (Safont, 2010). Therefore, several additional simulations focused on these influences to obtain a more comprehensive understanding of the elastic modulus at the nano level. Also, additional simulations including compressive and shear tests of the same original model were implemented to evaluate the elastic modulus from different perspectives.

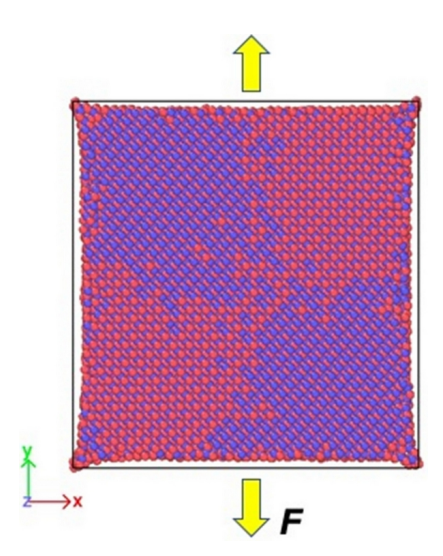


FIG. 3: Schematic of SiC tensile model

2.3 Simulation of Heat Conduction

LAMMPS provides a few different ways to evaluate thermal conductivity. Because the morphology of the material may affect the final result on a microscopic scale (Papanikolaou, 2008), both slab-like shapes and cubic shapes were investigated. Also, other possible factors influencing thermal conductivity, like the temperature and size of the model, were tested. In the case with a slab shape of SiC, depicted in Fig. 4, adding a heat flux into the model was straightforward. Energy and structure optimization was implemented to the entire system first. Then, with PBC applied in all three directions, the SiC thin slab was relaxed to a designated temperature under the NVE ensemble. After the whole system was stable, two thermostats were set up, one with energy added to become a hot region and the other with energy subtracted to become a cold region. The amount of energy added was equal to that of the energy subtracted, which resulted in a heat flux in between. Here, the basic idea is related to Fourier's law, which is given by

$$J = -\kappa \nabla T \tag{4}$$

where J is the local heat flux density, κ is the thermal conductivity, and ∇T is the temperature gradient along the latitudinal direction of the SiC slab. The temperature gradient was created by the heat flux mentioned above, where the same amount of heat was added and subtracted at each time step at the positions of 0.25L and 0.75L, respectively. Based on the slope of the temperature gradient profile, the thermal conductivity was derived.

In this work, the heat flux is defined as

$$J = \frac{\Delta E}{2A\Delta t} \tag{5}$$

where ΔE is the amount of heat added to or subtracted from the slab every Δt timestep, and A is the cross-sectional area of the slab. With the value of heat flux determined, the thermal conductivity can be calculated using Eq. (4).

When it comes to a cubic model, it is not appropriate to directly set up a hot region and cold region to continuously create energy flow in between due to the morphology of the model. Thus a different method called equilibrium Green-Kubo formalism was used in this scenario. The Green-Kubo formulas corresponding to the ensemble average of the autocorrelation for the thermal conductivity with respect to the heat flux can be written as

$$\kappa = \frac{V}{3k_B T^2} \int_{0}^{\infty} \langle J(0) \cdot J(t) \rangle dt$$
 (6)

where in the formula, V is the volume of the model; k_B is the Boltzmann constant, which is defined as $1.380649 \times 10^{-23} \text{ J} \cdot \text{K}^{-1}$; T is the temperature of the system; and J is the heat flux in the model. In the scenario of two-body interactions, the heat flux is expressed as

$$J = \frac{1}{V} \left[\sum_{i} e_{i} v_{i} - \sum_{i} S_{i} v_{i} \right] = \frac{1}{V} \left[\sum_{i} e_{i} v_{i} - \sum_{i < j} (F_{ij} \cdot v_{j}) r_{ij} \right] = \frac{1}{V} \left[\sum_{i} e_{i} v_{i} - \frac{1}{2} \sum_{i < j} (F_{ij} \cdot (v_{i} + v_{j})) r_{ij} \right]$$
(7)

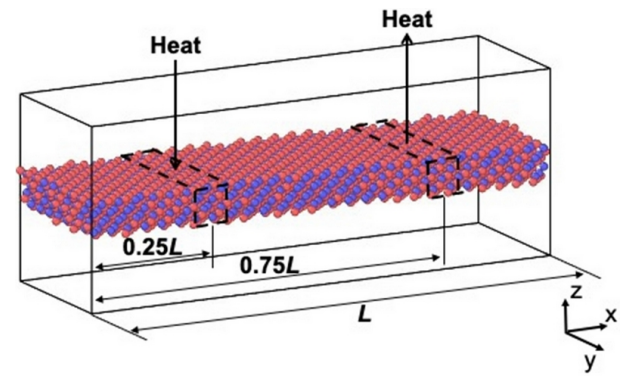


FIG. 4: Schematic of SiC thin-slab model with heat flux added

In the first term, e_i stands for the per-atom energy (kinetic energy and potential energy). In the second term, S_i is the per-atom stress tensor. The stress tensor multiplies v_i (velocity of the ith atom) as a 3 \times 3 matrix-vector that multiplies to yield a vector. F_{ij} indicates the force on atom i due to atom j and r_{ij} is the position between atom i and atom j.

3. RESULTS

3.1 Dry Friction of Silicon Carbide

3.1.1 Simulation Results of Asperity-Asperity Shear

The entire process of asperity-asperity shear, which is shown in Fig. 5, is visualized through Ovito. In Fig. 5, the horizontal axis represents the displacement or the moving distance of the upper asperity during the course of the simulation. For the two profiles, a friction force with a positive value indicates that a force is detected on the lower asperity and is directed toward the upper asperity horizontally. Similarly, a normal force with a negative value indicates that the two asperities are repelling each other in the vertical direction, while a positive value indicates attraction. It can be observed in Fig. 5 that the positions where two asperities first made contact, attractive interaction was dominated via the normal force. Due to the large oscillations in the instantaneous results, both friction and normal forces were averaged over the sliding distance to obtain an effective friction coefficient. Basically, it is the ratio of the summation of all the monitored forces during the contact and the total number of the forces through the procedure when the two materials were in contact for subsequent analysis, although such an operation hides the change of forces during the friction process.

3.1.2 Simulation Results of Asperity-Slab Shear

The profiles of friction force and normal force for asperity-slab shear are depicted in Fig. 6. On the curve of normal force versus displacement in Fig. 6, there was originally a downward force acting on the slab due to the squeezing between the asperity and the slab. As the asperity moved in the x-direction, serious wear took place on the asperity such that many atoms interacting with the slab were stripped from the asperity and remained on the surface of the slab. It led to a reduction of the normal force between the two objects, and the main type of interaction converted from repulsion to attraction at a point during the friction process. One possible issue in this simulation is that Vashishta potential may not provide an exactly flat surface when creating the lower SiC slab at high temperatures, but it is still acceptable.

3.1.3 Effect of Temperature

The temperature of a brake system is an extremely important factor, which can largely influence overall friction performance. A common range for the temperature of a brake system in an ordinary vehicle is about 300 K to

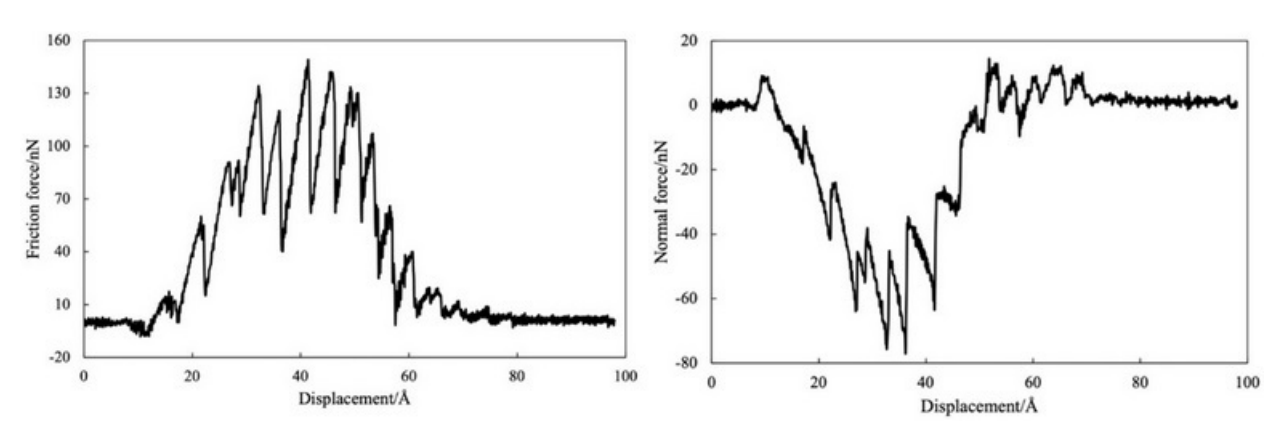


FIG. 5: Profiles of friction force and normal force versus displacement of upper asperity in asperity-asperity shear

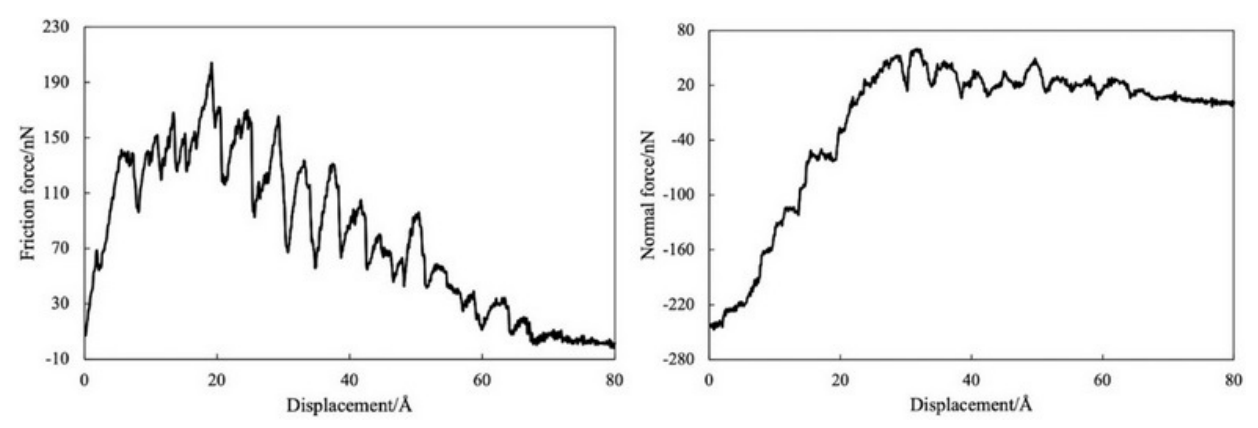


FIG. 6: Profiles of friction force and normal force versus displacement of upper asperity in asperity-slab shear

800 K. Using this temperature range, the two SiC asperities, each with a radius of 30 Å and normalized interference of 0.2, were used with the initial temperatures of 300 K, 400 K, 500 K, 600 K, 700 K, and 800 K. During the friction process the temperature was controlled to remain constant. The friction force, the normal force, and the corresponding coefficient of friction under each initial temperature for the two types of friction are shown in Fig. 7. Figure 7 indicates the trend of averaged friction force, averaged normal force, and effective friction coefficient for different initial temperatures in two kinds of friction processes. Figure 7(b) shows that with higher initial temperatures, friction force has a downward trend while normal force fluctuates only between 39 nN and 52 nN. This also leads to a decreasing trend in friction coefficient with higher initial temperatures. In fact, the atoms of SiC have large vibrations under such high temperatures, and this vibration can reduce their resistance to movement. Also, at high temperature the thermal softness would be more obvious and make the deformation of the asperity more easily (Yin et al., 2021). This could help make the asperity slide with a smaller force when atoms interact with each other.

It is worth noting that in asperity-asperity shear, the friction force drops because of the thermal effect at the initial temperature from 300 K to 600 K. However, when the initial temperature exceeds 600 K, the friction force increases. The main reason is that at high temperatures, more atoms from the two asperities gain high dynamic energy and come into contact with each other. This phenomenon not only causes more interactions that contribute to the adhesive force along the direction of motion, but also leads to more adhesive force in the vertical direction at an increasing temperature. Thus the friction coefficient shows a decreasing trend at first and a slight increase when the temperature rises. The wear between two asperities is more obvious as well at the high temperature. The friction coefficient values

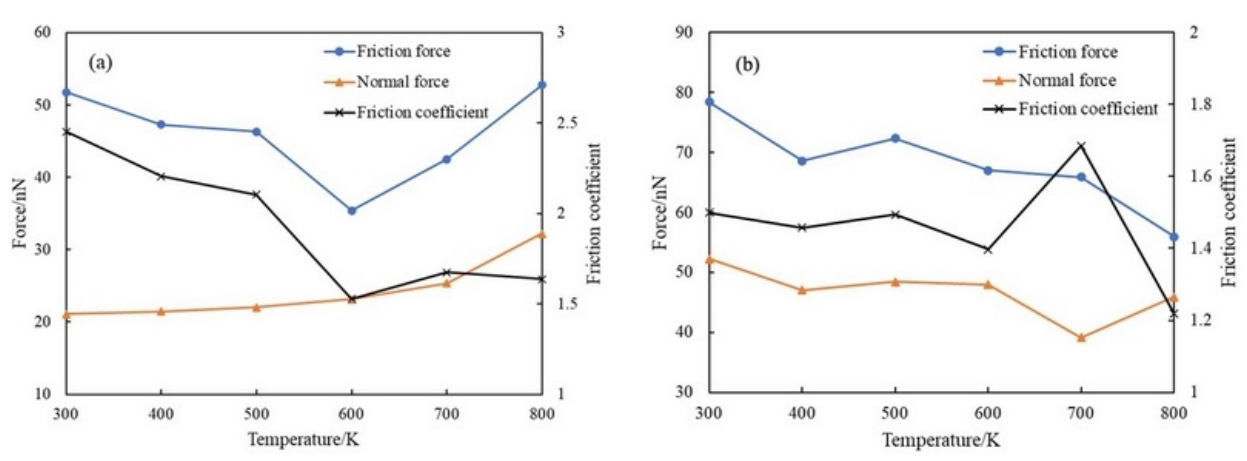


FIG. 7: Friction force, normal force, and corresponding friction coefficient versus initial temperature in (a) asperity-asperity shear and (b) asperity-slab shear

are all greater than 1, which may seem alarming at first. However, these values greater than unity are acceptable because, on a nanoscale, adhesive interaction is an important contribution to the friction force between atoms (Hu and Martini, 2015). Adhesive interaction among other factors increases the magnitude of the friction coefficient because the friction force increases.

3.1.4 Effect of Sliding Speed

The sliding speed between the brake pad and the disc was given as 10 m/s to 60 m/s with a 10 m/s increment to simulate the asperity friction process using the same interference, asperity radius, and initial temperatures as the previous section. The data derived from the simulation using a temperature of 300 K is exhibited in Fig. 8. From the result, it seems both friction force and normal force do not express any apparent trend with the change in sliding speed. The calculated effective friction coefficient changes only a small amount (2–2.5 for asperity-asperity shear and 1.1–1.5 for asperity-slab shear). This result indicates that the sliding speed at this scale does not have a significant influence on friction performance, which has an agreement with what Vadgama et al. (2015) found in the friction of copper asperities.

3.1.5 Effect of Asperity Intersection

With two asperities sliding relative to each other, the length of overlap in between could be a variable that affects the interaction among atoms, thus affecting the friction process. To evaluate this parameter, the interference between the asperities was divided by the radius of one asperity to obtain the normalized interference. Here, the asperity radius was the same as previous sections, which was 30 Å. The sliding speed was 10 m/s with 300 K as the initial temperature of the system. Note that in asperity-slab shear simulation, the normalized interference was defined as the vertical length compressed into the slab divided by the radius of the upper asperity. Different interference definitions result in different normal loads in asperity-slab shear.

Figure 9 illustrates how normalized interference influences the forces and the effective friction coefficient. Consider that on a nanoscale, there is also an attraction force between atoms. The initial normalized interference was set from -0.05 to 0.3 in the asperity-asperity friction with an interval of 0.05, and from 0 to 4/15 in the asperity-slab friction with an interval of 1/15; negative values indicate there is a gap vertically between the two asperities. Both friction force and normal force show increasing trends with more interference. Typically, the friction force would increase with more interference, since the number of atoms contacting each other would increase and cause larger adhesive forces between the two asperities. However, the normal force also exhibits an increasing trend as interference increases. By analyzing the change of the normal force and the visualization with each timestep, this anomaly can be explained by the higher repulsion between two asperities caused by larger interference. Further, based on the growth

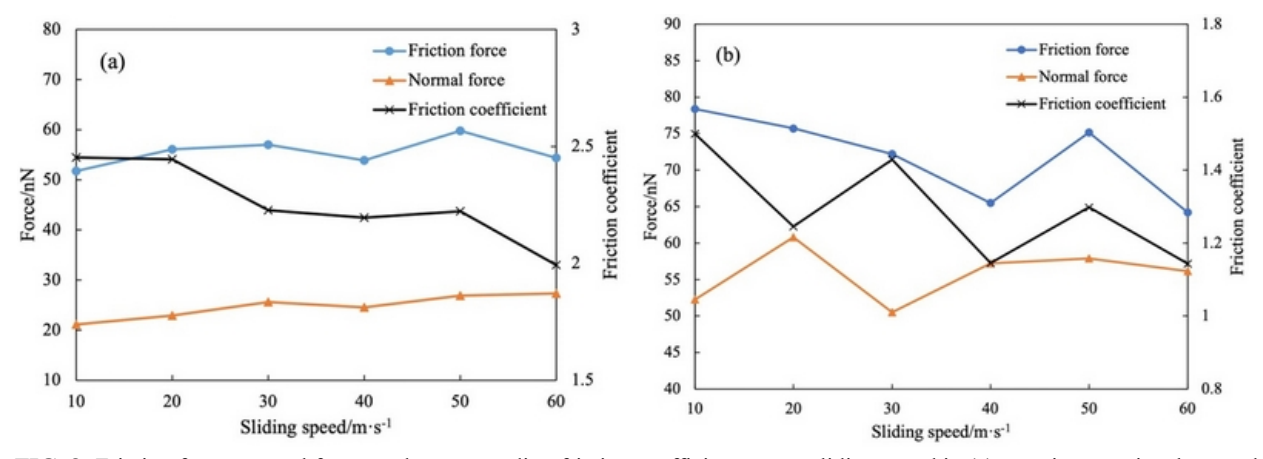


FIG. 8: Friction force, normal force, and corresponding friction coefficient versus sliding speed in (a) asperity-asperity shear and (b) asperity-slab shear

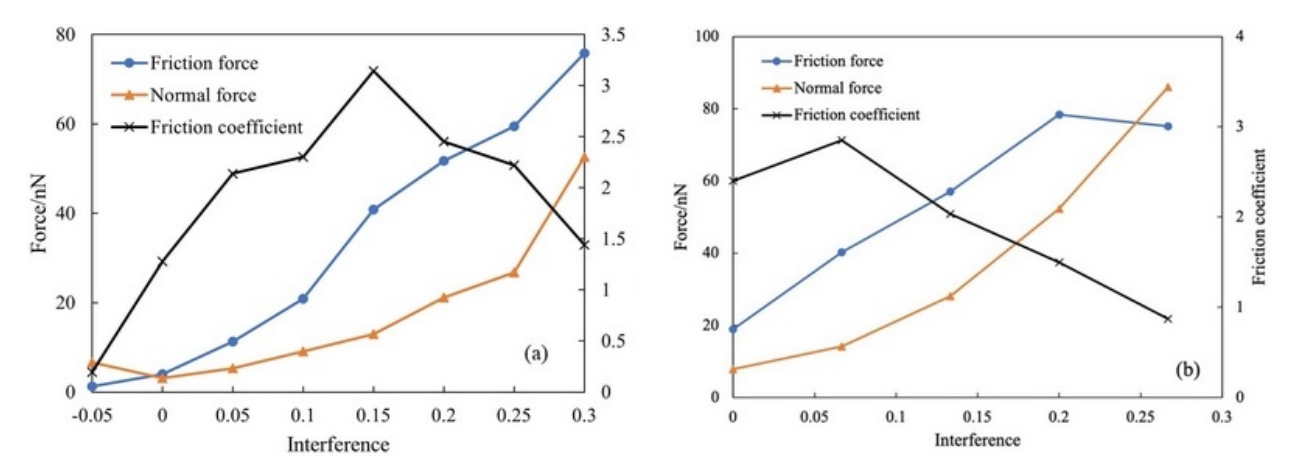


FIG. 9: Friction force, normal force, and corresponding friction coefficient versus normalized interference in (a) asperity-asperity shear and (b) asperity-slab shear

rates of the two forces, the calculated friction coefficient first rises then falls, which shows that the friction force grew faster than the normal force, and later the situation was reversed.

3.1.6 Effect of Asperity Size

Particle size can influence friction as well, because with larger radius asperities, there would be an increase in the number of atoms interacting with each other during the friction process, leading to a larger friction force. This is clearly shown in Fig. 10. The asperity radius for each simulation was 20, 30, 40, 50, and 60 Å for asperity-asperity shear and 20, 30, 40, and 50 Å for asperity-slab shear; sliding speed was 10 m/s; initial temperature was 300 K; and a normalized interference of 0.2. The results show that both friction force and normal force increased with increasing asperity size. It is evident that the interaction between larger asperities caused more contact among atoms, leading to higher acting forces. The friction coefficient was thereby reduced because of the faster increase of normal force than friction force.

3.1.7 Effect of Crystalline Lattice Orientation

In order to evaluate the effect lattice orientation has on two friction types, different angles of lattice were tested. The result is shown in Fig. 11. The lattice orientations of 0° , 5° , 10° , 15° , 20° , 25° , 30° , 35° , 40° , and 45° were

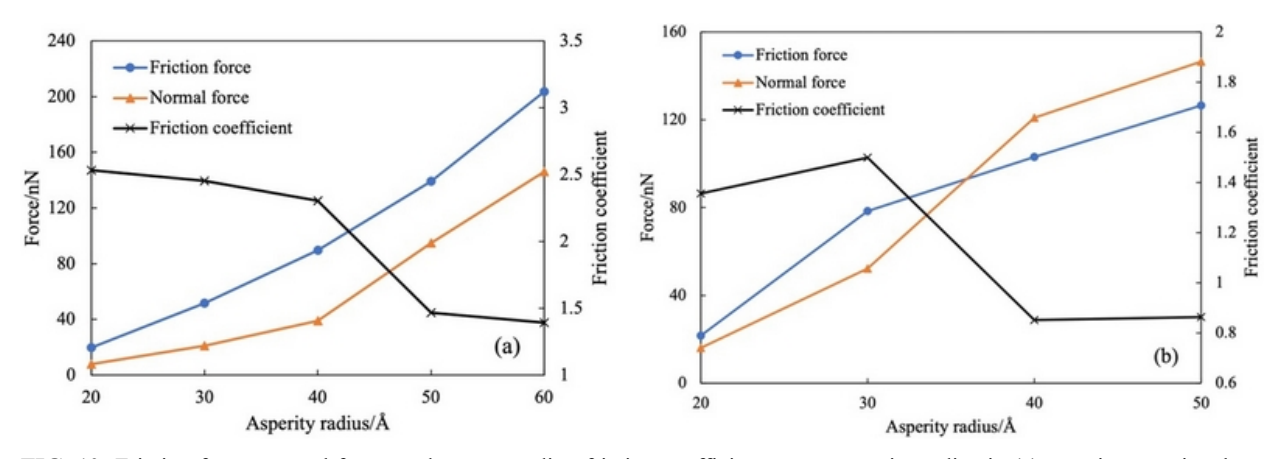


FIG. 10: Friction force, normal force, and corresponding friction coefficient versus asperity radius in (a) asperity-asperity shear and (b) asperity-slab shear

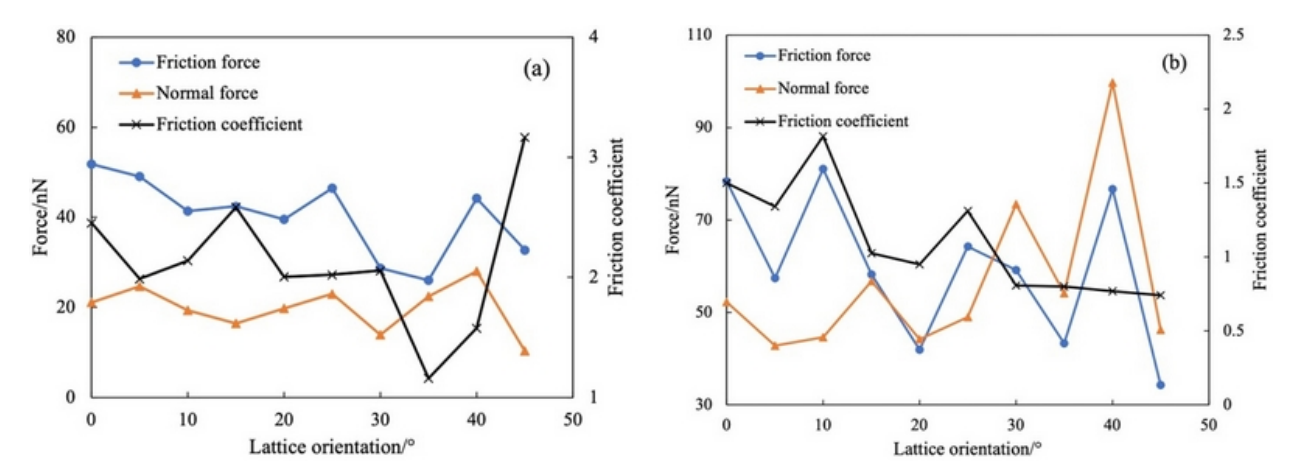


FIG. 11: Friction force, normal force, and corresponding friction coefficient versus lattice orientation in (a) asperity-asperity shear and (b) asperity-slab shear

used. Different from the work done by Vadgama et al. (2015), the results here indicate there is no clear relationship between forces and lattice orientation for SiC either on asperity-asperity friction or asperity-slab friction. However, when it comes to 45°, the interaction is weaker than other orientations, which is similar to a lattice orientation of 0°, but with a relatively small value (maximal value 50 nN for 0° and 20 nN for 45° in the asperity-asperity shear; maximal value 78 nN for 0° and 34 nN for 45° in the asperity-slab shear). It also turns out that the frictional wear was enhanced significantly between 5° and 40° compared to 0° and 45°. Based on this analysis and the observation of the visualization of friction, the reason for large friction wear and the conversion from repulsive force to attractive force comes from higher deformation and material transfer due to the lattice orientation being not close to the sliding plane (111), which is more prone to slip (Chen et al., 2007; Zhao et al., 2021). A comparison between a 45° orientation and 25° orientation can be seen in Fig. 12. When the lattice orientation is 45°, the deformation or the material transfer of the asperities is much lower than the case of 25°. This results in lower wear and forces because the 45° orientation is more parallel to the (111) plane.

3.1.8 Wear Rate

In the friction simulation, both friction materials in contact generate debris, which is in a similar situation as Fig. 12. The debris is the adhesive atoms transferred from one friction material to the other. Based on this, the wear rate can be evaluated via the following equation:

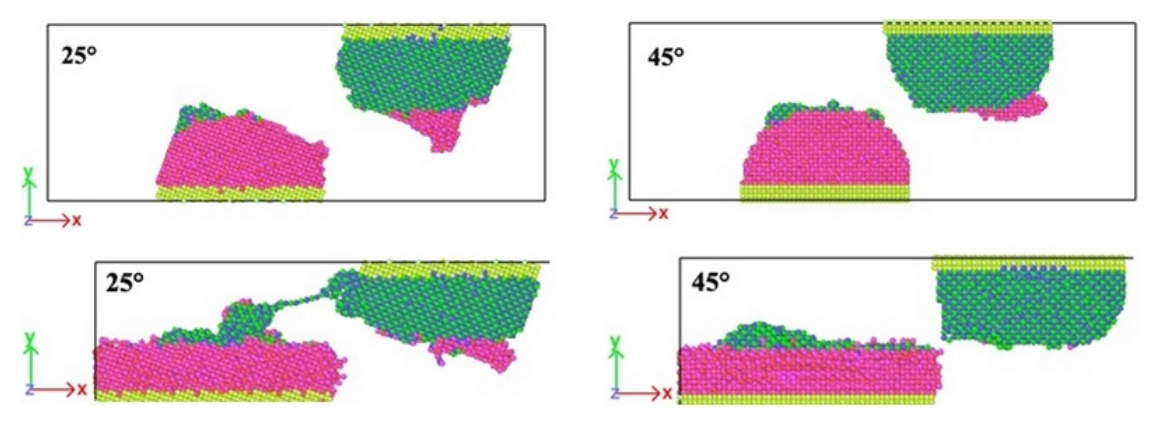


FIG. 12: Deformation after friction for 25° and 45° lattice orientations

$$W = \frac{M_d}{L} \tag{8}$$

Here, W is the wear rate, M_d is the relative atomic mass of the debris, and L is the friction length of the asperity. The results of the wear rate of the sliding system involving various temperatures, sliding speeds, interferences, and asperity sizes in both asperity-asperity friction and asperity-slab friction simulations is shown in Fig. 13. In all four scenarios in the figure, it appears that the asperity-slab friction always has relatively higher wear rate than the asperity-asperity friction. Also, by analyzing the wear rates of both contact surfaces, the asperity in the asperity-slab friction tends to produce more debris than the slab as well as the asperities in asperity-asperity friction. At temperatures from 300 K to 800 K, the wear rate of the asperity-asperity contact exhibits a slight decrease, while the wear rate of the asperity-slab friction shows an increasing trend. One observation from the asperity-slab friction is that the high temperature makes the atoms easier to move and separate from each other in the asperity. This results in an increase in the worn atoms. In the asperity-asperity contact, however, it is easier for the frictional force from one asperity to push the atoms of the other asperity forward, and the relocated atoms would come to a stop at a new location but still touch the initial asperity. Therefore, the number of worn atoms does not have an obvious growth. A sliding speed between 10 m/s and 80 m/s does not seem to be a factor affecting the wear rate for the asperity-asperity contact, but in the asperity-slab friction the wear rate substantially increases when the sliding speed changes from 10-30 m/s to 40-80 m/s. At a higher sliding speed, the asperity cannot maintain its shape and it deforms significantly, leading to more worn atoms. As for the interference and the asperity size, a larger interference or asperity radius would give rise to a higher wear rate since more atoms are in contact with each other.

Figure 14 shows the wear rates of the upper asperity, lower asperity, and the total wear rate in both shear types. Similar to the conclusions we obtained previously, when the lattice orientation is not aligned with the sliding direction

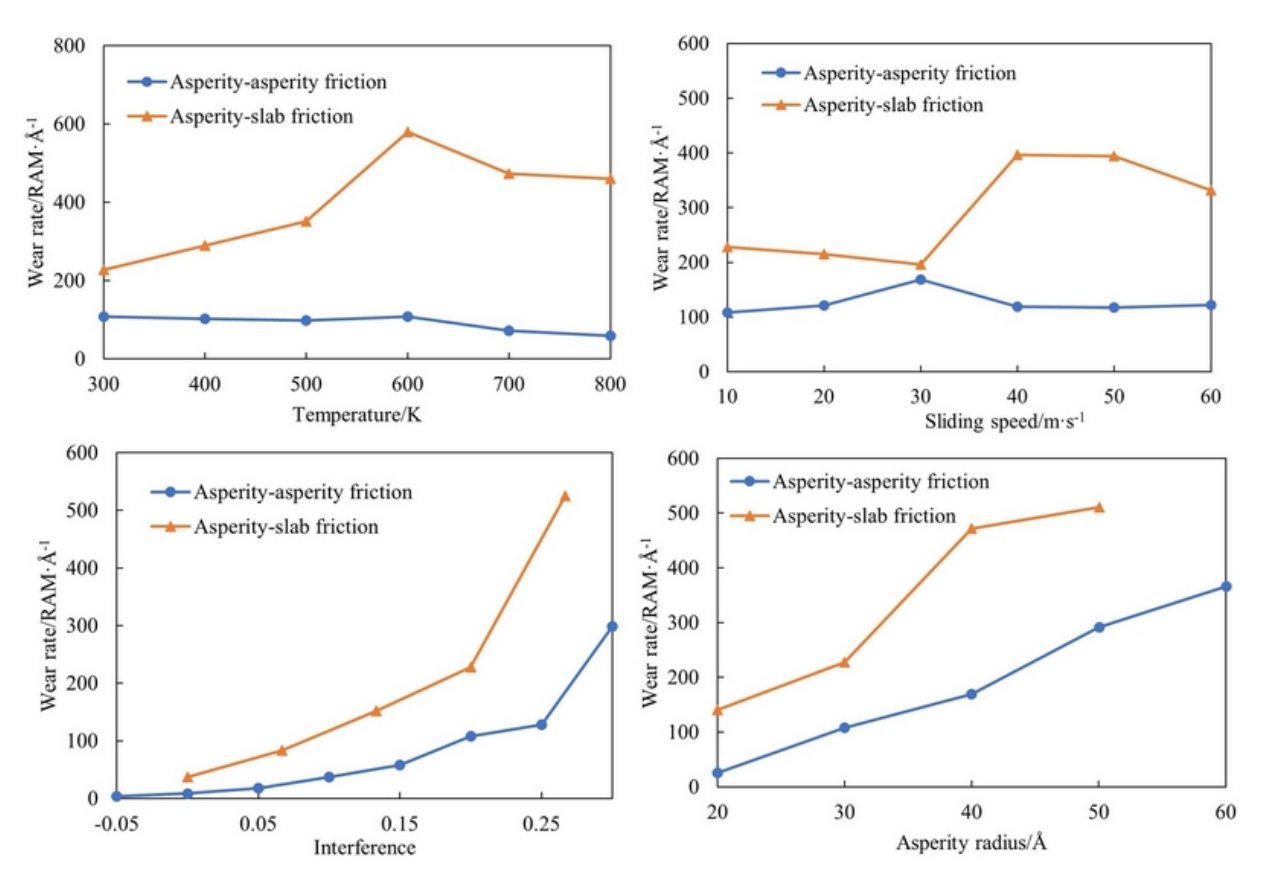


FIG. 13: Wear rate of the sliding system involving various temperatures, sliding speeds, interferences, and asperity radius in both asperity-asperity shear and asperity-slab shear

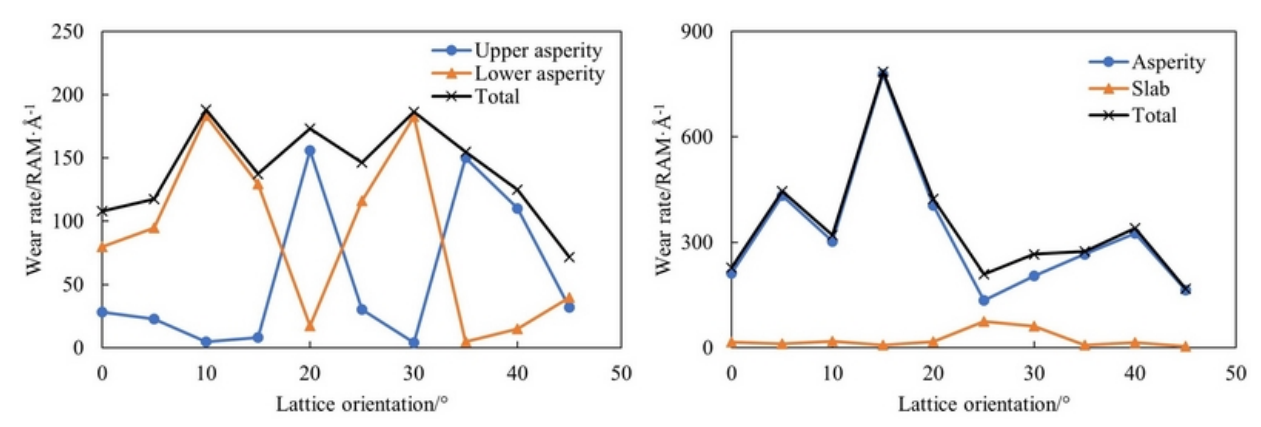


FIG. 14: Wear rate of each contact surface and total wear rate with various lattice orientations in asperity-asperity shear and asperity-slab shear

 $(5^{\circ}-40^{\circ})$, the friction materials undergo more resistance and generate more debris. When the lattice orientation is close to or the same as the sliding direction $(0^{\circ}$ and $45^{\circ})$, a smaller wear rate can be obtained. It is also interesting to see that with the lattice orientation between 5° and 40° , one of the asperities is severely worn, while the other one is relatively less worn. With the lattice orientations of 0° and 45° , the wear rates of the two contact surfaces are at the same level. However, in the asperity-slab contact, the asperity always produces more worn atoms than the slab.

3.1.9 Validation of Simulation Results for Tribological Properties

Table 1 compares the results with some similar works, where Cases 2–5 are from the literature, and Case 1 is the result obtained from this investigation. Apparently, those derived from the MD simulations are local friction coefficients since they are computed from the atomistic friction response at the asperity level, whereas the experimental result in Case 2 is the global friction coefficient obtained on the macroscale. Although there is no direct data that can be used to examine the validity of the result of the friction simulation in this work, it is possible to see that the results derived from the MD simulation are always greater than those from the experimental results. In Case 3, a higher load was applied, leading to the generation of grooves during frictional sliding, whereas there were no grooves in Case 2. The generation of grooves indicates that the material experienced obvious plastic deformation by a large ploughing force (thus a large frictional force). This is the exact reason why the friction coefficient was much higher in Case 3 than in Case 2. We have a similar observation in our MD simulation, even though the size scale is at the atomic level. The MD model shows that the SiC asperities undergo severe plastic deformation in both asperity-asperity and asperity-slab frictional contact conditions. In asperity-asperity contact, for example, the ploughing frictional force is much greater than the other force components. Meanwhile we obtained larger friction coefficients in asperity-asperity friction than those from asperity-slab friction. Therefore, we believe that the simulation results derived in the present work are reasonable.

On the macroscale, the tribological theory calculates the friction coefficient considering both ploughing and adhesion (Hopkins and Moore, 2013). However, there is also some research that points out that the third contribution,

Case	Materials	Shape	Туре	Temperature	Load	Sliding speed (m/s)	Friction coefficient
1	SiC	Asperity	MD	300 K	21.1 nN	10	2.45
2 (Zhang et al., 2020)	SiC	Ring	Experiment	Ambient	6.6 N	0.897	0.2
3 (Zhang et al., 2020)	SiC	Ring	Experiment	Ambient	27 N	0.897	0.8
4 (Vadgama et al., 2015)	Cu	Asperity	MD	300 K	13.5 nN	10	2.25
5 (Chien et al., 2016)	Cu	Block	MD	293 K	150.96 nN	100	2.3

TABLE 1: Friction coefficient from selected bodies of work

which is the accumulation of the chip in front of the upper asperity during friction, cannot be ignored on a nanoscale (Zhu et al., 2011). The final friction coefficient would be the sum of all three contributions just mentioned. On the nanoscale, the adhesion could be more significant due to the attractions among the atoms as mentioned previously. In addition, if the dimension of the simulation model is inconsistent with the macroscopic spatial scales—that is to say, if parts of the model feature different spatial scales—then the final result could be largely affected by the finite size effect (Leyva-Mendivil et al., 2016). This is possibly why the total friction coefficient is always much larger on the nanoscale than on the macroscale. In fact, it is not unusual to obtain a frictional coefficient greater than 1 from MD simulation.

3.2 Elastic Modulus of Silicon Carbide

3.2.1 Simulation of Tensile Test

During the tensile test simulations, there was no significant change in the appearance of the block at first, then it became obvious, with the formation of a neck or fracture, that deformation was occurring somewhere along the length of the sample. The tensile test simulations with strain rates of 0.005 ps^{-1} , 0.01 ps^{-1} , and 0.02 ps^{-1} were conducted to examine the effect of strain rate on elastic modulus. The dimension of the SiC block model was about $20 \text{ Å} \times 20 \text{ Å} \times 6 \text{ Å}$. The outputs of the three scenarios are gathered in Fig. 15. From the slope of the stress–strain curves in the elastic region, the elastic modulus for 0.005 ps^{-1} , 0.01 ps^{-1} , and 0.02 ps^{-1} was calculated to be about 261.73 GPa, 251.14 GPa, and 261.5 GPa, respectively. Since the data calculated was averaged after the simulation, there could be some errors in the final result, but overall, the elastic modulus does not change with strain rate, even though the yield strength and ultimate tensile strength do vary with strain rate.

Similarly, to evaluate the size effect on the elastic modulus of SiC blocks at the atomic level, two types of modifications were applied to change the size of the model: first was to change the length of the block only in the x-direction, and second was to change its length in both x- and y-directions. It is apparent that the change in length both in a single direction and two directions show very similar effects on the slope of the stress–strain curve during elastic deformation. The elastic modulus increased from 270.95 GPa to 290.81 GPa then 313.61 GPa as the original length of the model in the x-direction increased from 20 Å to 40 Å then 60 Å, respectively. When both the lengths in x-and y-directions increased with the same magnitude, the curves for each case exhibited the same tendency of growth in slope, which was 270.95 GPa to 292.76 GPa then 310.82 GPa, before the transformation from elastic deformation to plastic deformation. A larger model could have a higher elastic modulus with similar shapes. Figure 16 exhibits

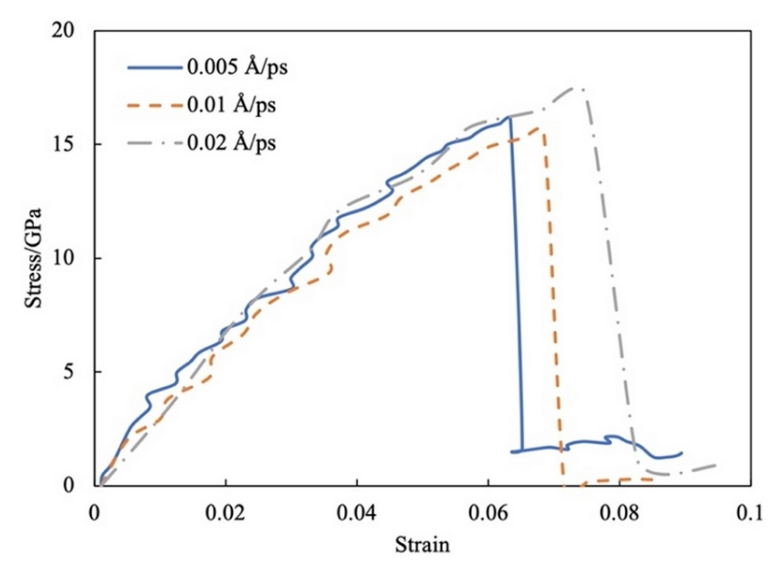


FIG. 15: Stress-strain curves for SiC block at different strain rates

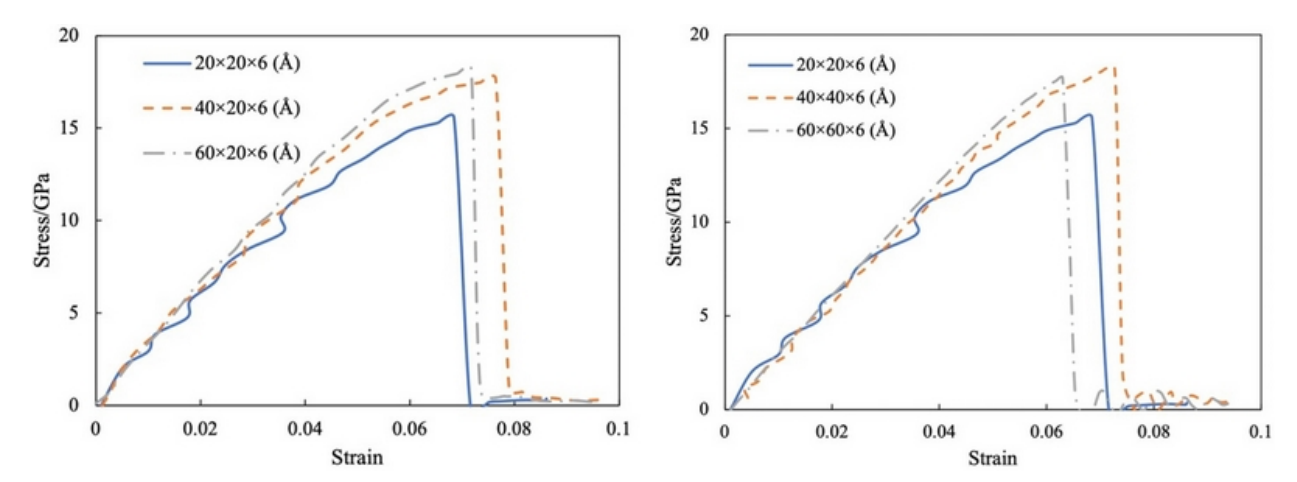


FIG. 16: Stress-strain curves for SiC blocks of different sizes with the graph on the left changing in only the x-direction, and the graph on the right changing in both x- and y-directions

the stress–stain curves of SiC blocks with different sizes. From the tensile test simulation, Poisson's ratio of SiC can be calculated as well. However, the script used in the tensile test fixed both of the two sides of the SiC model, which makes it harder to derive transverse strain. Thus an alternative approach was applied on the same original model in LAMMPS. In this approach, the simulation box was allowed to change its shape and/or volume during the simulation such that Poisson's ratio could be derived by calculating the ratio between transverse strain and axial strain. At the beginning of the simulation, the change in transverse strain was unstable and was not used in calculation. The Poisson's ratio with the change in axial strain is depicted in Fig. 17. The final averaged Poisson's ratio from Fig. 17 is about 0.15.

3.2.2 Simulation of Compression and Shear Tests

The simulation of both compression and shear were completed using the same model, which was $20 \text{ Å} \times 20 \text{ Å} \times 6 \text{ Å}$ with a strain rate of 0.01 ps^{-1} and a temperature of 300 K. The stress–strain curves are shown in Fig. 18. The elastic

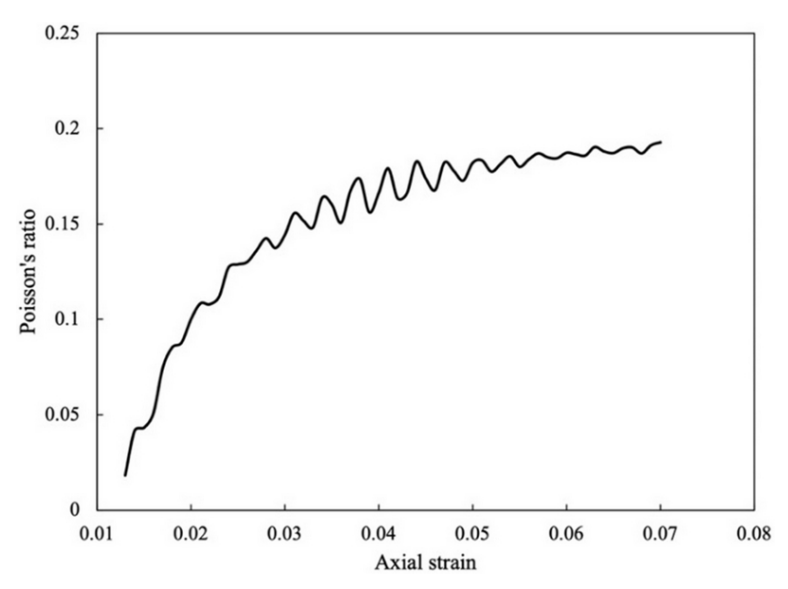


FIG. 17: Poisson's ratio of SiC versus axial strain

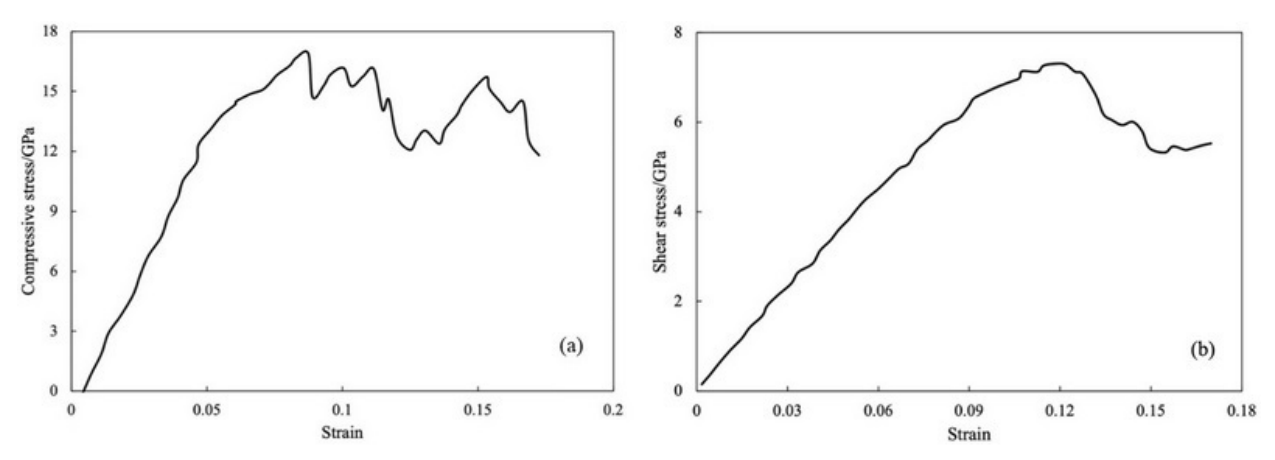


FIG. 18: Stress-strain curves for SiC blocks in (a) compression and (b) shear

modulus derived from the compression simulation is approximately 276.79 GPa, which is very close to the result from the previous tensile test. The shear modulus is about 72.63 GPa, which is much lower than Young's modulus obtained from both tensile and compressive tests.

3.2.3 Validation of Simulation for Mechanical Properties

Table 2 lists the results derived from the simulation (Case 1) and other works (Cases 2–6). The comparison shows that the elastic modulus of this work is different from those in Cases 3 and 5. However, the one obtained from a larger model size in this paper is comparable to the results reported in Cases 2 and 4, and it is also very close to Case 3 even though Case 3 deals with α -SiC, from both simulation and experiment. Based on this discovery, the size effect could be overcome with large dimensions, resulting in an elastic modulus close to the real value. The literature also points out that the size effect may not be negligible when the characteristic length of the model shrinks down to several nanometers (Wang et al., 2012). For example, in Case 3, the elastic modulus and tensile strength of the thin film 3C-SiC varies a lot with the thickness, which indicates that the dimension of the model is an important factor to mechanical properties at nanoscale. The difference of the results between Case 3 and our simulation may be induced by the different potentials, different dimensions, and different methods used. In addition, the literature reported that the lattice orientation has a remarkable effect on the elastic modulus of 3C-SiC as well (Goel et al., 2013). And the value estimated along the [100] direction is usually lower than in other directions (Pabst et al., 2012). Poisson's ratio of SiC from the literature is between 0.142 and 0.16, which also shows an agreement with the result in this work (Pierson et al., 1996; Sömiya and Inomata, 1991). For compression and shear simulations, a similar stress-strain relationship can be found in the literature, indicating similar elastic modulus and strength compared to the present work (Chavoshi and Xu, 2018). Although there are no direct experimental data found about the elastic modulus of the compressive test, a literature reported an elastic modulus of 325 ± 8 GPa by using nanoindentation to 3C-SiC thin film, which is close to the value from our tensile test (Nawaz et al., 2019). This again indicates that the dimension

TABLE 2: Elastic modulus from selected bodies of work				
Case	Material	Type	Elastic modulus (GPa)	
1	β-SiC	MD	270.95–313.61	
2 (Vashishta et al., 2007)	β-SiC	MD	313.6	
3 (Wang et al., 2012)	β-SiC	MD	370–490	
4 (Vashishta et al., 2007)	α-SiC	MD	323.4	
5 (Vashishta et al., 2007)	β-SiC	Experiment	314.2	
6 (Harris, 1995)	β-SiC	Experiment	392–448	

of the model affects the calculated modulus significantly. The shear modulus found from the literature (Zawawi et al., 2019; Wang et al., 2017) has a range of 24.78–250 GPa, which is comparable to the result obtained from the present work (72.63 GPa). These methods of testing mechanical properties such as elastic modulus may help study their relationship to tribological properties and provide new ideas for improving tribological performance.

3.3 Thermal Conductivity of Silicon Carbide: Simulation Results and Validation

SiC slabs with dimensions of 117.7092 Å \times 34.8768 Å \times 9 Å, 239.778 Å \times 34.8768 Å \times 9 Å, and 357.4872 Å \times 34.8768 $\text{Å} \times 9$ Å were employed in this simulation. The cross-sectional area was known for each case. Every 1000 timesteps (Δt), 80×0.00431 eV (ΔE) was added and subtracted from the slab. The system was first constructed and relaxed at 100 K. Then the heat flux was introduced to the system. The heat flux simulation in the thin-slab SiC gives the temperature distribution along the slab shown in Fig. 19. The maximum point corresponds to where the heat was added and the minimum point corresponds to where the heat was subtracted. Then based on the slope of the temperature variance between hot and cold regions, the thermal conductivity could be interpolated. The system was heated from 100 K to 900 K with steps of 200 K. What needs to be noted is that although the trend of thermal conductivity for different relaxation times could be similar, the heat flux at the beginning of the relaxation may not have reached a stable state yet. This would result in inaccurate estimations of thermal conductivity. So, a longer relaxation time is favored. An 8 ns relaxation was applied to each stage so that the heat flux would remain stable. The value of thermal conductivity of the SiC slab along the x-direction versus temperature is shown in Fig. 20. It turns out that from the beginning of the simulation, when the heat flux just formed, to the time of 8 ns, when the heat flux had reached a stable state, approximately, the measured thermal conductivity didn't change much, aside from dropping very fast from a relatively high value to a low level as the temperature increased from 100 K to 300 K. Then it remained stable while the temperature kept increasing to 900 K. The results from different sized slabs didn't show an obvious difference either. According to literature (Lessel et al., 2013), there could be an influence of finite size effects regarding the phonon mean free path. It states that when the length of heat flux is shorter than maximum phonon mean free path, the material always behaves as if it had a higher thermal conductivity with a longer mean free path. This effect would disappear once the heat flux length exceeds the maximum phonon mean free path. Based on this theory, it is likely the sizes of the models in all three cases were beyond the maximum phonon mean free path such that no significant difference is observed on thermal conductivity values.

The relationship between thermal conductivity and temperature are shown in Fig. 20 and can be explained by phonon kinetic theory (Liu et al., 2017). The theory gives the formula as

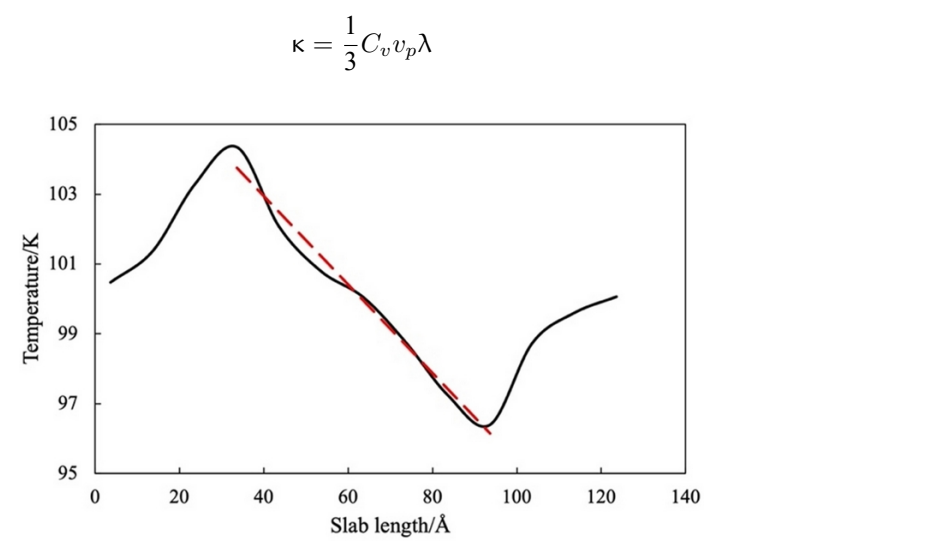


FIG. 19: Temperature distribution of SiC slab at 100 K

(9)

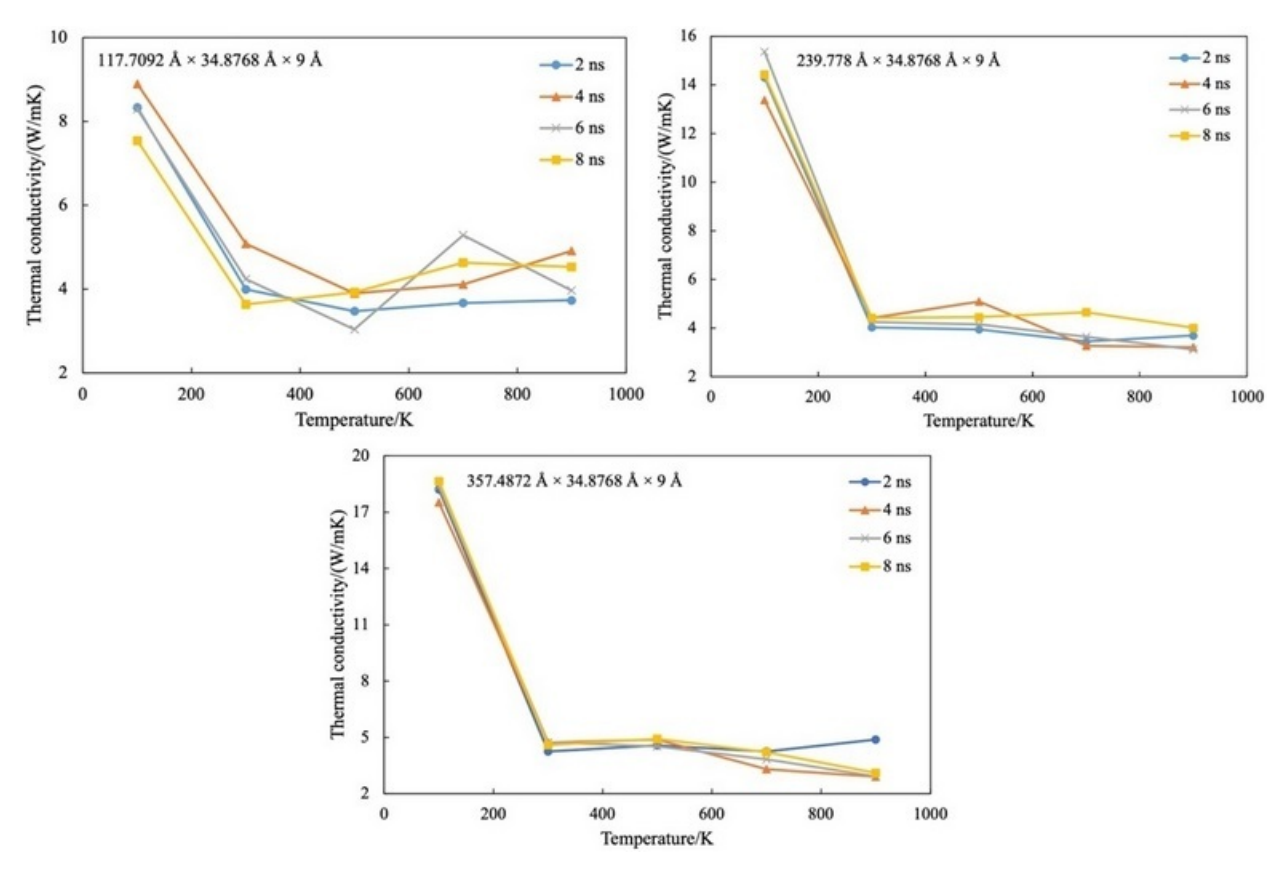


FIG. 20: Thermal conductivity of SiC slab along x-direction versus temperature at different relaxation times

where C_v is the specific heat at constant volume, v_p is the average phonon velocity, and λ is the phonon mean free path. Usually, v_p is a constant, and λ decreases as temperature goes up (Tritt, 2004). When the temperature is very low, C_v is proportional to the cubic of temperature. When the temperature increases, C_v approaches a constant while λ continues to decrease. That is why thermal conductivity has a huge drop in the low-temperature region, and a decreasing trend when temperature increases. The simulated thermal conductivities at 300 K and 500 K agree well with the data reported in the literature, as shown in Table 3.

Cubic SiC, another common configuration, was considered in the work of thermal conductivity evaluation. The sizes of $3 \times 3 \times 3$ and $5 \times 5 \times 5$ (lattice constant) were used with a Green-Kubo equilibrium MD method to calculate thermal conductivity from 100 K to 900 K with steps of 100 K. Figure 21 shows the result after curve fitting. There is a huge difference in magnitude of thermal conductivity between cubic SiC and SiC thin slab with the same material and potential. This indicates the magnitude of thermal conductivity for SiC is related to the shape of the material. The thermal conductivity of cubic SiC decreases from about 267.64 W/mK at 100 K to about 28.33 W/mK at 900 K for the small model. For the larger model, in the low-temperature range, there is an obvious difference in magnitude, but

TABLE 3: Thermal conductivity of 3C-SiC nanowire from selected bodies of work

Case	Model	Temperature (K)	Thermal conductivity (W/mK)	
1	This work	300; 500	3.8-4.9; 4-5	
2 (Cao et al., 2013)	3C-SiC nanowire with 6×8 unit cell	300; 500	5; 4	
3 (Papanikolaou, 2008)	3C-SiC nanowire with 7×7 unit cell	500	3.7–4.2 (Si termination),	
	3C-SiC hallowire with 7 × 7 thirt cen	300	4.4–5.3 (C termination)	

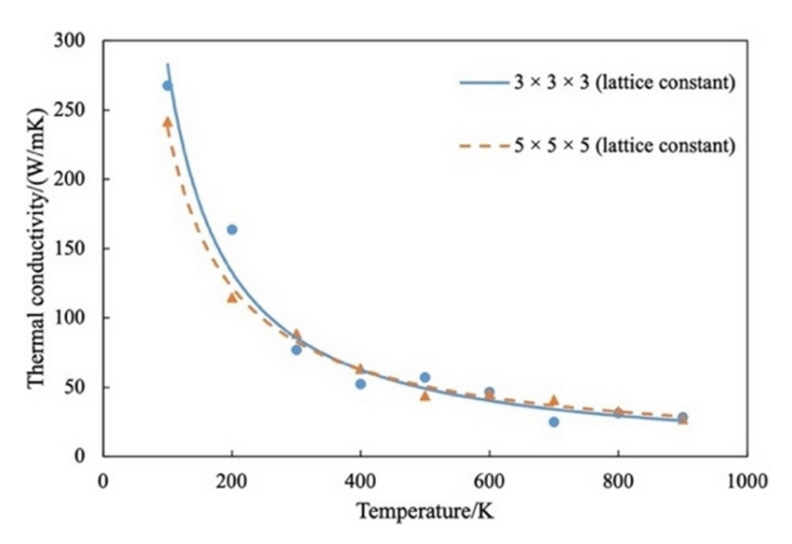


FIG. 21: Thermal conductivity of cubic SiC at various temperatures

in the high-temperature range the results from the two models are approximately equivalent. We can also interpolate the value of thermal conductivity for this specific model at different temperatures after curve fitting. There is a huge reduction of thermal conductivity from cubic SiC to SiC thin slab due to boundary scattering, phonon leakage, and related interactions even though the thin slab is in atomically perfect condition in this scenario. In practice, compared to bulk single materials, the synthesis technologies for making thin-slab materials can reduce thermal conductivity as well by introducing more impurities, disorder, and grain boundaries (Prasad et al., 2017).

This trend is similar to the results reported by other works; however, the magnitude is slightly different. This could be due to different potentials and sizes of the models used (Szpunar et al., 2018; Li et al., 1998). Some comparisons are shown in Table 4: Case 1 is the result in this work; Case 2, using GW02 potential, and Case 3, being done in a real experiment, are from literature. The fact that our result is lower than the literature results could be because the dimension of the simulation model is not large enough to obtain a converged value of thermal conductivity (Schelling et al., 2002). It should also be pointed out that the classical MD simulation does not include the quantum effect. Although it can be negligible when the temperature is very high, quantum effect on phonon scattering would be significant at low temperature (Wu and Hsu, 2009). This effect is not considered in this work but will be studied in the future.

4. CONCLUSIONS

In this paper a MD study of the mechanical, tribological, and thermal properties of 3C-SiC was performed using LAMMPS. Our main conclusions are listed below:

1. On the nanoscale, the dominant factors affecting the tribological properties of friction materials not only include the shear forces between the contact pairs but also the adhesive forces due to the attractions between atoms. The influence from the wear debris due to plastic deformation is also nonnegligible at the atomic level.

TABLE 4: Thermal conductivity of cubic 3C-SiC from selected bodies of work

Case	300 K (W/mK)	600 K (W/mK)	900 K (W/mK)
1	76.80–88.72	45.07–46.63	27.15–28.33
2 (Szpunar et al., 2018)	230	110	60
3 (Senor et al., 1996)	_	95–103	75

- 2. The computational result of the effective friction coefficient by taking the ratio of the shear force and the normal force was found to be in the range of 0.3–3.3 for asperity-asperity shear and 0.7–3.0 for asperity-slab shear. These results are consistent with the existing data found in the literature. In addition, the wear rates of both shear configurations were estimated and analyzed to assist the understanding of the tribological properties.
- 3. The tensile test of SiC on a nanoscale indicates that the strain rate could be related to the plastic deformation rather than elastic deformation. An increase in the model size leads to a higher Young's modulus due to the scaling effect. The estimated Young's modulus is 270.95–313.61 GPa based on the tensile test simulation and 276.79 GPa based on the compressive test simulation. The estimated shear modulus is 72.63 GPa and Poisson's ratio is 0.15, accordingly.
- 4. The selection of the geometry also plays an important role in the computation of thermal conductivities. A thin slab has a much lower thermal conductivity compared to a cubic SiC. The thermal conductivity decreases with temperature for both geometric shapes. It is found that the rate of decrease is much higher at a lower temperature range than at a higher temperature range, indicating that the thermal conductivity remains stable at higher temperatures. In 3C-SiC thin slab, the thermal conductivity ranges from approximately 8 to 18 W/mK to 4 W/mK with an increase in the temperature. In cubic 3C-SiC, it shows a similar relationship with the temperature but results in higher values from 250 W/mK to 30 W/mK.
- 5. During the simulations of asperity friction, mechanical testing, and thermal analysis, the Vashishta potential works better than the other potential functions. However, this same potential may not work well on flat surfaces at high temperatures.

Future work will potentially be a direct modeling of the instabilities induced by the interaction between the thermal process and the contact forces on the nanoscale via a MD simulation approach.

ACKNOWLEDGMENT

Support for this work, provided by the National Science Foundation under Contract (No. 1928876), is gratefully acknowledged.

REFERENCES

- Cao, H.C., Wang, Z., and Guan, H.W., Molecular Dynamics Simulation of Thermal Conductivity of 3C-SiC Nanowire, *Adv. Mat. Res.*, vol. **800**, pp. 210–212, 2013.
- Chavoshi, S.Z. and Xu, S.Z., Tension-Compression Asymmetry in Plasticity of Nanotwinned 3C-SiC Nanocrystals, *J. Appl. Phys.*, vol. **124**, p. 95103, 2018.
- Chen, H.P., Kalia, R.K., and Nakano, A., Multimillion-Atom Nanoindentation Simulation of Crystalline Silicon Carbide: Orientation Dependence and Anisotropic Pileup, *J. Appl. Phys.*, vol. **102**, pp. 063514-1–063514-9, 2007.
- Chien, C.H., Wang, C.T., and Tsai, C.H., Temperature Effect on Kinetic Friction Characteristics of Cu Substrate Composed by Single Crystal and Polycrystalline Structures, *Comput. Mater. Sci.*, vol. 117, pp. 412–421, 2016.
- Gao, J.P., Luedtke, W.D., and Gourdon, D., Frictional Forces and Amontons' Law: From the Molecular to the Macroscopic Scale, *J. Phys. Chem. B*, vol. **108**, pp. 3410–3425, 2004.
- Goel, S., Stukowski, A., and Luo, X.C., Anisotropy of Single-Crystal 3C-SiC during Nanometric Cutting, *Model. Simul. Mat. Sci. Eng.*, vol. **21**, p. 65004, 2013.
- Harris, G.L., Properties of Silicon Carbide, London: INSPEC, 1995.
- Hopkins, D.W. and Moore, D.F., *Principles and Applications of Tribology: Pergamon International Library of Science, Technology, Engineering and Social Studies: International Series in Materials Science and Technology*, Pergamon Press, 2013.
- Hu, X.L. and Martini, A., Atomistic Simulation of the Effect of Roughness on Nanoscale Wear, *Comput. Mater. Sci.*, vol. **102**, pp. 208–212, 2015.

Lessel, M., Loskill, P., and Hausen, F., Impact of van der Waals Interactions on Single Asperity Friction, *Phys. Rev. Lett.*, vol. 111, p. 035502, 2013.

- Leyva-Mendivil, M.F., Lengiewicz, J., and Page, A., Skin Microstructure Is a Key Contributor to Its Friction Behaviour, *Tribol. Lett.*, vol. **65**, pp. 1–17, 2016.
- Li, J., Porter, L., and Yip, S., Atomistic Modeling of Finite-Temperature Properties of Crystalline β-SiC: II. Thermal Conductivity and Effects of Point Defects, *J. Nucl. Mater.*, vol. **255**, pp. 139–152, 1998.
- Li, Y.Y., Li, Y., and Xiao, W., Point Defects and Grain Boundary Effects on Tensile Strength of 3C-SiC Studied by Molecular Dynamics Simulations, *Nucl. Eng. Technol.*, vol. **51**, pp. 769–775, 2019.
- Liu, Q.F., Luo, H., and Wang, L., Tuning the Thermal Conductivity of Silicon Carbide by Twin Boundary: A Molecular Dynamics Study, *J. Phys. D Appl. Phys.*, vol. **50**, p. 65108, 2017.
- Lu, Y.F., A Combinatorial Approach for Automotive Friction Materials: Effects of Ingredients on Friction Performance, *Compos. Sci. Tech.*, vol. **66**, pp. 591–598, 2006.
- Mao, Y.C., Li, Y.Y., and Xiong, Y.H., Point Defect Effects on the Thermal Conductivity of β-SiC by Molecular Dynamics Simulations, *Comput. Mater. Sci.*, vol. **152**, pp. 300–307, 2018.
- Nawaz, A., Islam, B., and Mao, W.G., Nanoscale Elastic-Plastic Deformation and Mechanical Properties of 3C-SiC Thin Film Using Nanoindentation, *Int. J. Appl. Ceram. Technol.*, vol. **16**, pp. 706–717, 2019.
- Pabst, O., Schiffer, M., and Obermeier, E., Measurement of Young's Modulus and Residual Stress of Thin SiC Layers for MEMS High Temperature Applications, *Microsyst. Technol.: Sensors, Actuators, Systems Integration*, vol. 18, pp. 945–953, 2012.
- Papanikolaou, N., Lattice Thermal Conductivity of SiC Nanowires, J. Phys. Condens. Matter, vol. 20, p. 135201, 2008.
- Pierson, H.O., Herring, R.B., and Hunt, L.P., Handbook of Refractory Carbides and Nitrides: Properties, Characteristics, Processing and Applications, New York: Elsevier Science & Technology Books, 1996.
- Plimpton, S., Fast Parallel Algorithms for Short-Range Molecular Dynamics, J. Comput. Phys., vol. 117, pp. 1–19, 1995.
- Prasad, V., Jaluria, Y., and Zhang, Z.M., Annual Review of Heat Transfer XX, New York: Begell House Publishing, 2017.
- Rahnejat, H., Tribology and Dynamics of Engine and Powertrain: Fundamentals, Applications and Future Trends, Cambridge: Elsevier Science & Technology, 2010.
- Safont, C.G., Mechanical Properties at Nano-Level, *Universitat Politècnica de Catalunya*, from https://recercat.cat/handle/2072/182097, 2010.
- Sanguineti, A., Samela, A., and Rampinelli, F., Cementitious-Based Brake Pads Technology: Performance, Low Energy Consumption, Emission Drop, SAE Tech. Paper 2018-01-1867, 2018. DOI: 10.4271/2018-01-1867
- Sato, T., Ishida, T., and Jalabert, L., Real-Time Transmission Electron Microscope Observation of Nanofriction at a Single Ag Asperity, *Nanotechnology*, vol. **23**, p. 505701, 2012.
- Schelling, P.K., Phillpot, S.R., and Keblinski P., Comparison of Atomic-Level Simulation Methods for Computing Thermal Conductivity, *Phys. Rev. B Condens. Matter Mater. Phys.*, vol. **65**, 2002.
- Senor, D.J., Youngblood, G.E., and Moore, C.E., Effects of Neutron Irradiation on Thermal Conductivity of SiC-Based Composites and Monolithic Ceramics, *Fusion Sci. Technol.*, vol. **30**, p. 943, 1996.
- Sharma, S., Molecular Dynamics Simulation of Nanocomposites Using BIOVIA Materials Studio, Lammps and Gromacs (Micro and Nano Technologies Series), San Diego, CA: Elsevier, 2019.
- Si, L., Wang, X.L., and Xie, G.X., Nano-Adhesion and Friction of Multi-Asperity Contact: A Molecular Dynamics Simulation Study, *Surf. Interface Anal.*, vol. 47, pp. 919–925, 2015.
- Solomon, D.G. and Berhan, M.N., Characterization of Friction Material Formulations for Brake Pads, in *Proceedings of the World Congress on Engineering Vol II WCE 2007*, London, U.K., July 2–4, 2007.
- Sömiya, S. and Inomata, Y., Silicon Carbide Ceramics—1: Fundamental and Solid Reaction, Dordrecht, Netherlands: Springer, 1991.
- Sriwiboon, M., Tiempan, N., and Kaewlob, K., Non-Asbestos Organic (NAO) Disc Pad Wear Behavior: Divergence of Thickness Loss and Weight Loss, SAE Tech. Paper 2018-01-1866, 2018. DOI: 10.4271/2018-01-1866
- Stukowski, A., Visualization and Analysis of Atomistic Simulation Data with OVITO—The Open Visualization Tool, *Model. Simul. Mat. Sci. Eng.*, vol. 18, p. 015012, 2010.
- Szpunar, B., Malakkal, L., and Rahman, J., Atomistic Modeling of Thermo-Mechanical Properties of Cubic SiC, *J. Am. Ceram. Soc.*, vol. **101**, pp. 4753–4762, 2018.

- Tritt, T.M., Thermal Conductivity: Theory, Properties, and Applications, New York: Kluwer Academic/Plenum Publishers, 2004.
- Vadgama, B.N., Jackson, R.L., and Harris, D.K., Molecular Scale Analysis of Dry Sliding Copper Asperities, App. Nanosci., vol. 5, pp. 469–480, 2015.
- Vashishta, P., Kalia, R.K., and Nakano, A., Interaction Potential for Silicon Carbide: A Molecular Dynamics Study of Elastic Constants and Vibrational Density of States for Crystalline and Amorphous Silicon Carbide, J. Phys., vol. 101, p. 103515, 2007.
- Wang, L., Liu, Q.F., and Yu, W.S., Shear Response of β-SiC Bulk Dependent on Temperature and Strain Rate, *Acta Mech. Solida Sin.*, vol. **30**, pp. 137–144, 2017.
- Wang, W.X., Niu, L.S., and Zhang, Y.Y., Tensile Mechanical Behaviors of Cubic Silicon Carbide Thin Films, Comput. Mater. Sci., vol. 62, pp. 195–202, 2012.
- Wang, Z.G., Zu, X.T., and Gao, F., Atomistic Simulations of the Mechanical Properties of Silicon Carbide Nanowires, *Phys. Rev. B Condens. Matter*, vol. 77, 2008.
- Wu, M.C.H. and Hsu, J.Y., Thermal Conductivity of Carbon Nanotubes with Quantum Correction via Heat Capacity, *Nanotechnology*, vol. 20, p. 145401, 2009.
- Yi, Y.B., Perturbation Methods in Thermoelastic Instability (TEI) with Finite Element Implementation, in *Encyclopedia of Thermal Stresses*, Dordrecht, the Netherlands: Springer, pp. 3635–3641, 2014.
- Yin, Z.H., Zhu, P.Z., and Li, B.Z., Study of Nanoscale Wear of SiC/Al Nanocomposites Using Molecular Dynamics Simulations, Tribol. Lett., vol. 69, p. 38, 2021.
- Zawawi, S.A., Hamzah, A.A., and Majlis, B.Y., Nanoindentation of Cubic Silicon Carbide on Silicon Film, *Jpn. J. Appl. Phys.*, vol. **58**, p. 51006, 2019.
- Zhang, W., Yamashita, S., and Kita, H., Progress in Tribological Research of SiC Ceramics in Unlubricated Sliding—A Review, Mater. Des., vol. 190, p. 108528, 2020.
- Zhao, J.X., Ma, B., and Li, H.Y., Investigation of Thermoelastic Instabilities of Wet Clutches, 2013 IEEE International Symposium on Assembly and Manufacturing (ISAM), 2013.
- Zhao, L., Zhang, J.J., and Pfetzing, J., Depth-Sensing Ductile and Brittle Deformation in 3C-SiC under Berkovich Nanoindentation, *Mater. Des.*, vol. 197, p. 109223, 2021.
- Zhong, J., Adams, J.B., and Hector, L.G., Molecular Dynamics Simulations of Asperity Shear in Aluminum, *J. App. Phys.*, vol. **94**, pp. 4306–4314, 2003.
- Zhou, Y., Hirao, K., and Yamauchi, Y., Tribological Properties of Silicon Carbide and Silicon Carbide-Graphite Composite Ceramics in Sliding Contact, *J. Am. Ceram. Soc.*, vol. **86**, no. 6, pp. 991–1002, 2003.
- Zhu, P.Z., Hu, Y.Z., and Ma, T.B., Molecular Dynamics Study on Friction Due to Ploughing and Adhesion in Nanometric Scratching Process, *Tribol. Lett.*, vol. **41**, pp. 41–46, 2011.